Dynamical epidemic suppression using stochastic prediction and control

Ira B. Schwartz

Plasma Physics Division, Code 6792, Naval Research Laboratory, Washington, DC 20375, USA

Lora Billings

Department of Mathematical Sciences, Montclair State University, Montclair, New Jersey 07043, USA

Erik M. Bollt

Department of Mathematics and Computer Science, Clarkson University, Potsdam, New York 13699, USA
and Department of Physics, Clarkson University, Potsdam, New York 13699, USA

We consider the effects of noise on a model of epidemic outbreaks, where the outbreaks appear randomly. Using a constructive transition approach that predicts large outbreaks prior to their occurrence, we derive an adaptive control scheme that prevents large outbreaks from occurring. The theory is applicable to a wide range of stochastic processes with underlying deterministic structure.

I. INTRODUCTION

Recently, there has been much research of steady state epidemics in random populations [1] and their control [2]. Nonequilibrium diseases, in contrast, are those diseases exhibiting outbreaks that fluctuate in time. Childhood [3,4] and tropical diseases [5,6] are a few examples of outbreaks having strong annual oscillations with random amplitude. In modeling the annual incidence of infections, random components from the environment and/or populations play a significant role [7,8]. While excellent data from seasonally fluctuating diseases illustrate strong annual oscillations with random peak outbreaks in the infections [4,9], models and data analysis reveal that outbreaks stem from stochastic perturbations in either population or epidemic parameters, making deterministic prediction difficult.

Predictability of seasonally driven diseases that are stochastic is necessary for the application of methods to suppress future outbreaks. Many vaccine schemes are available for equilibrium diseases [3,10], but in the case of nonequilibrium outbreaks, current methods may enhance outbreaks or fail to achieve their goals [11,12]. (Similar problems arise in the large fluctuation theory of stochastic dynamical systems [13].) Other methods pulse the population without sampling for prediction [14], or they rely on reducing spread via mean threshold reduction [3]. To address the problem of suppressing outbreaks in stochastic epidemics, we apply a mathematical method [15] to a stochastic model to predict outbreaks before they occur, and then adapt a vaccine strategy which prevents the outbreak from occurring. The theory exploits a transition probability description from small amplitude incidence to outbreak dynamics, and generates a region of high probability transport of the most sensitive regions to stochastic effects. Moreover, it allows us to monitor regions of stochastic dynamics that have a high probability of preceding a large outbreak, which in turn leads to a design of a vaccine control strategy to suppress outbreaks. We thus argue a general simple, but effective, control technique that takes advantage of complicated interactions of determinism and

noise. The techniques introduced here may also be applied to general stochastic nonautonomous systems of the form

$$\frac{dx}{dt} = G(x,t) + \eta(t), \tag{1}$$

where $G(x,t)=G(x,t+1)$, and the noise is added periodically with the period of drive, i.e.,

$$\eta(t) = \eta_n \Delta(t-n), n=1,2,\ldots, \tag{2}$$

Δ is the Dirac delta function, and η_n is now a discrete random variable. The form of Eq. (1) allows us to consider the dynamics as a discrete-time constantly perturbed stochastic dynamical system.

II. A STOCHASTIC EPIDEMIC MODEL

A standard system used to study and predict the stochastic dynamics of disease epidemics is based on a simplified reduced version of the well-known SEIR (defined below) compartmental model [7,9,16], known as the modified SI model [17]. In deterministic settings, the system has been exploited to model single and coupled patch populations [18], as well as testing vaccine strategies [14,19]. Assume that the population is sufficiently large so that the various subgroups are assumed to be continuous. The population dynamics is described by susceptible $S(t)$; exposed, but not yet infectious, $E(t)$; infective $I(t)$. The recovered $R(t)$ class in the model can be derived from model results since $S+E+I+R=1$ [17].

Seasonality is input into the model via the contact rate, $\beta(t)$, so we let $\beta(t)=\beta_0(1+\delta \cos 2\pi t)$, where $0 \leqslant \delta < 1$. Other parameters used to quantify the dynamics are a sceptible input rate μ (which includes the birth rate, as well as a possible fixed vaccine control), the mean latent period, α^{-1}, and the infectious period, γ^{-1}. The full deterministic rate equations are given by

$$\frac{dS(t)}{dt} = \mu[1 + h(t)] - \beta(t)SI - \mu S,$$

$$\frac{dE(t)}{dt} = \beta(t)SI - \alpha E - \mu E,$$

$$\frac{dI(t)}{dt} = \alpha E - \gamma I - \mu I, \tag{3}$$

$$R(t) = 1 - [S(t) + E(t) + I(t)],$$

where $h(t)$ is a small perturbation used for vaccination. That is, when $h(t)$ is negative, the input of susceptibles into the system is reduced. Since it will be designed to be adaptive stochastic control, $h(t)$ will also depend on the state variables.

For realistic childhood disease parameters chosen here, theoretical [20] and numerical analysis [17] show that for almost all cases, the infective and exposed population follow each other in time to first order, leading to a reduction which describes a modified SI model (MSI), given by

$$\frac{dS(t)}{dt} = \mu[1 + h(t)] - \mu S(t) - \beta(t)I(t)S(t),$$

$$\frac{dI(t)}{dt} = \left(\frac{\alpha}{\mu + \gamma}\right)\beta(t)I(t)S(t) - (\mu + \alpha)I(t). \tag{4}$$

The parameters used for measles data [20] are given by μ =0.02, α=1/0.0279, γ=1/0.01, β_0=1575, and δ=0.095, and are fixed throughout the paper. Here, the parameter $h(t)$ is a time-dependent vaccine control whose value we will calculate adaptively, and depends on the phase space location of $(S(t),I(t))$.

Following the discretized stochastic model in Eq. (1), we strobe the system with period-1 to create a Poincaré map. Without loss of generality, we define a discrete stochastic model for the purposes of this paper [21]. Using a discrete stochastic map approach will allow us to make careful and accurate interpretations in terms of the $(S(t),I(t))$ variables, as well as to examine the interaction of the dynamics and control with the underlying topology of the system. We consider the uncontrolled stochastic system (h=0) as a two-dimensional map F of a region D into itself

$$(S,I)(t + 1) = F[(S,I)(t)] + \eta(t), \tag{5}$$

where η is a two-dimensional random variable having a normal distribution given by $v(x)=e^{-(x^T\Sigma^{-1}x)/2}/(2\pi\|\Sigma\|^{1/2})$, with Σ=diag (σ^2), and we choose the standard deviation to be σ =0.035. Since the two-dimensional deterministic system has an attractor with unequally-sized components, the noise amplitude is scaled so that it is defined on the unit square. Because the standard deviation is based on the rescaled coordinates, it is small compared to the attractor size and is smaller than the modulation component of the contact rate in Eq. (4). A typical time series of the I component is shown in Fig. 1. Notice the frequent aperiodic bursts, which for the chosen parameters of the deterministic part of the model, Eq. (4), would not occur were it not for the random perturbations in Eq. (5); the deterministic and stochastic parts interact in a fundamental way to create complicated oscillations that ei-
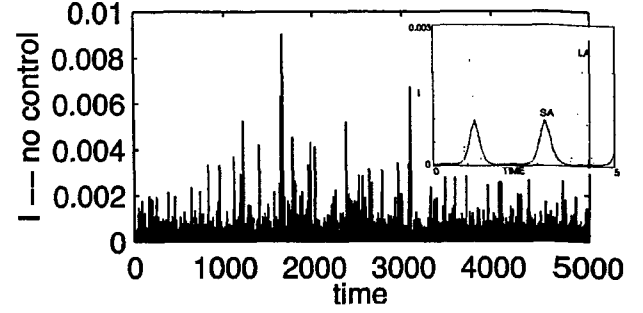

FIG. 1. This is an uncontrolled time series of the fraction of infectives I for the MSI model under random forcing in Eqs. (4) and (5). The parameters are given in the text. Inset: Note the small (SA) period 2 and large (LA) period 3 amplitude oscillations of the underlying bistable deterministic system. No chaos is present when $\eta(t)$=0, and the system only exhibits periodic SA or LA oscillations.

ther phenomenon could not create on their own.

Notice that in the absence of any stochastic fluctuations $[\eta(t) \equiv 0]$, the system will settle down to one of two periodic solutions. The two stable solutions are plotted in the Fig. 1 inset. The period 2 cycle has a small amplitude (SA) while the period 3 cycle is of large amplitude (LA). However, as seen from the time series in the figure, outbreaks, which occur due to stochastic fluctuations, may have enhanced amplitudes by almost an order of magnitude over the period 3 cycle.

Although the system is stochastic, its dynamics may be quantified in terms of Lyapunov exponents by spatial integration against the invariant density [22]. For the parameters used to generate the time series in Fig. 1, we compute the Lyapunov exponents, and find them to be λ_1=0.1638 and λ_2=−0.4853. These values, together with the evidence of nearly intersecting stable and unstable manifolds [23], indicate a completed horseshoe dynamics under the influence of the noise, described as stochastic chaos [8,15]. However, the completed horseshoe dynamics, indicative of chaos in deterministic systems, is a geometric way of thinking about the interaction of noise and the underlying manifold structure of the deterministic part. The chaotic-looking dynamics are the result of mixing two stable attractors, while sampling unstable dynamics between them. The positive Lyapunov exponent is therefore a way of measuring contributions to the stochastic attractor of dynamics tracking near unstable manifolds. The fraction of time spent near the unstable manifolds, as well as the transition probabilities of the dynamics switching from small to large amplitude behavior may be explained by taking a dynamic probabilistic approach, which we sketch briefly. A full mathematical description is given in [15].

III. DISCRETE STOCHASTIC DYNAMICS AND TRANSITION PROBABILITIES

If the noise is continuous, we can compute the evolution of the probability density using a Fokker-Planck approach [24]. However, since the approach is one of discrete noise as in Eq. (1), we evolve the densities discretely as well. That is,

since the solution to the periodically driven is computed every period to form the discrete map, we do the same with the density.

We assume the noise comes from a distribution, $\nu(x)$. The evolution of an initial probability density function (PDF), $\rho : D \subset R^2 \rightarrow R$, is defined by the stochastic Frobenius-Perron operator [15] $P_F : L^1(R^2) \rightarrow L^1(R^2)$, given by

$$P_F(\rho(x)) = \int_D \nu[x - F(y)]\rho(y)dy. \qquad (6)$$

The density is invariant if it is a fixed point of the operator. This approach allows an approximation of the probabilistic transitions of one part of phase space to another [15] as well as the invariant density [25].

To compute the transition probabilities from one region of phase space to another, we discretize the region D of phase space. Specifically, we assume there exists a cover of the region D by disjoint sets B_i,

$$D = \bigcup_{i=1}^{N} B_i. \qquad (7)$$

Defining the set of characteristic basis functions,

$$\psi_i(x) = \chi_{B_i}(x) \equiv \begin{cases} 1, & x \in B_i \\ 0, & x \notin B_i \end{cases} \qquad (8)$$

allows one to generate finite dimensional projections of transport by computing the $N \times N$ matrix entries of a transition probability matrix [8,15] given by the equation

$$M_{i,j} = \int_D P_F(\psi_i(x))\psi_j(x)dx. \qquad (9)$$

Therefore, Eq. (9) yields the probability of transporting mass from box B_i to B_j.

In considering the problem of predicting stochastic outbreaks in the MSI model, we wish to compute the transition from a small amplitude (SA) oscillation to a large amplitude (LA) outbreak in a time series, such as the one generated in Fig. 1. The inset shows the deterministic periodic orbits of SA and LA, although noise may generate much larger outbreaks than the deterministic LA orbit. Stochastic perturbations of SA in the inset are approximately the same amplitude, and therefore are used as a threshold to define large outbreaks. The mass flux entries generated by Eq. (9) can be combined with the invariant density to generate the conditional probability of transition from set B_i to B_j, given B_i. A representation of the transition probability is depicted in Fig. 2. Notice that the most active transport regions lie close to a stable manifold of an LA orbit (period 3 saddle) in the underlying deterministic system. This stable manifold is the deterministic basin boundary which separates the SA (period 2) and LA (period 3) regular orbits of Eq. (4), and the coloring denotes the degree and location where this pseudobarrier is overcome due to noise. Notice that near each of the basin boundary saddles of period 3, transition to an outbreak is likely. However, the highest transition region is not near any saddle. Rather, the probability of an outbreak in this region is solely due to the interaction of the noise and the global topology of the underlying deterministic dynamics.

IV. ACTIVE CONTROL OF STOCHASTIC OUTBREAKS

For deterministic systems, normal methods of vaccine control will reduce the input rate of susceptibles. The value of h is usually computed so that at equilibrium (no seasonal forcing, or $\delta=0$), the net rate of production of infectives in one infectious period is less than unity. Under these conditions, the disease will die out. However, control of small amplitude oscillations in the periodically driven case can be done, but the disease will persist [26].

In the stochastic case in the presence of periodic drives, constant controls may make the problem worse. In Fig. 3, we see a direct comparison of constant vaccine control and no control. Notice that although the mean level of outbreaks appear to be reduced, the large fluctuations are greater than without control. Therefore, constant vaccine control, although sometimes the only guide, may increase the size of large outbreaks. Therefore, it is natural to try to sample and control discretelywhen considering stochastic outbreaks.

Vaccine activation using a variable h depends on finding the regions where an outbreak is most likely upon the next iteration. These are points of the trajectory generated by Eq. (5) in the SA basin that precede iterates in the LA basin. Although we compute conditional outbreaks from the spatial averages using the transition matrix, this is verified temporally. Using an uncontrolled stochastic time series of 50 000 iterates, and checking in which basin (SA or LA) each iterate is located, we show in Fig. 4 the most likely preoutbreak regions. In comparison to Fig. 2, the spatial average predicts similar transport regions of high conditional probability of the SA-LA transition.

We now define a bull's eye (BE) region to be an open connected neighborhood having high probability of transition from SA to LA outbreaks. The BE region, for a chosen threshold, is clearly shown in red in Fig. 2. Distinguishing the center point x_c, the BE region includes a neighborhood of radius ϵ that has a probability greater than a given threshold. Notice that this is not the only region in which transition occurs. Monitoring the BE region alone, therefore, is not sufficient for prediction of transitions [27]. However, it can be used to determine other regions that are not obvious for transition to an outbreak.

We can use the BE region as a first guess to monitor the dynamics. Let $x_0 \in E$ be the current point of the observed dynamics, and x_L a desired target point in the transport space close to the image of E, but in a region of lower transition probability. The relationship between the current point in the trajectory x_0 and the center of the bull's eye x_c is $x_0 = x_c + y$ for some y. To move the image of x_0 closer to the target point x_L, we activate the control parameter h in Eq. (4). By Taylor expansion about $F(x_c, \mu)$ when $h=0$ and ignoring higher order terms, we solve

$$h = \frac{[x_L - F(x_c, \mu) - \partial_x F(x_c, \mu)y]^T \partial_\mu F(x_c, \mu)}{\|\partial_\mu F(x_c, \mu)\|^2}, \qquad (10)$$

assuming $\partial_\mu F(x_c, \mu) \neq 0$. This control strategy is designed to target a desired region of lower probability, given the iterates
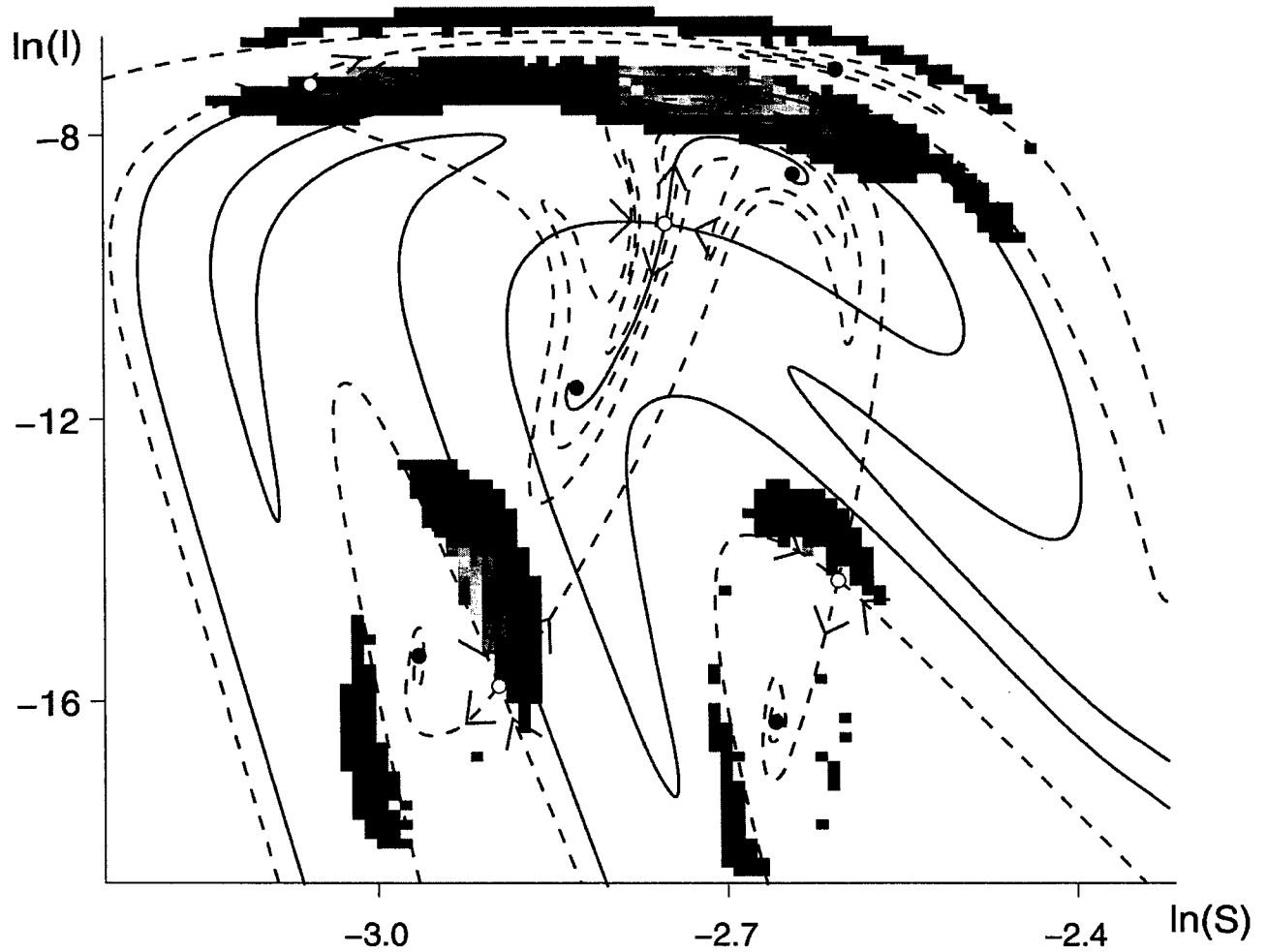
FIG. 2. (Color) The GTM result of the conditional probability of transition from small amplitudes to large outbreaks using the same parameters as in Fig. 1. The highest probability regions of transport (red) point to a bull's eye monitoring region for control. Overlaid are the stable and unstable manifolds corresponding to the underlying deterministic model.

land in a region of high transition probability.

Now we apply control to suppress large amplitude outbreaks. Focusing on points in a neighborhood of the BE region has the disadvantage that the values of I are already fairly large. Therefore, we use the detection region of the neighborhood around the (deterministic) preimage of the bull's eye, $F^{-1}(E, \mu)$, shown as an ellipse in Fig. 4. Using Eq. (10), the image of the ellipse, I_h, is found to be the figure eight shown in Fig. 4. We targeted a region in I_h which is close to the BE region but has a very low transition probability. Our techniques successfully steer trajectories away from the bull's eye region towards SA behavior by using only vaccine perturbations that control the flow of susceptibles about some mean value.

One advantage of choosing the detection region to be the preimage of BE is for relatively low values for the number of infected individuals (I), a prediction can be made about the future increase and steps can be taken to avert these dynamics. The perturbations represent a vaccination program, taking the form of $\mu_{new} = \mu[1 + h(t)]$. If h is negative, then more vaccinations are required to reduce the rate of susceptible individuals being introduced into the population. An example

of the success of this algorithm is shown in Fig. 5. On average, perturbations are applied 25–30 % of the time. Notice the maximum amplitude in comparison to the uncontrolled dynamics of Fig. 1. For this example, the Lyapunov exponents are $\lambda_1 = 0.0794$ and $\lambda_2 = -0.3764$, where the maximum exponent has been significantly decreased.

V. DISCUSSION

Stochastic bursting is present in many systems that are based on population dynamic modeling. In general, when such systems are subject to periodic forcing, there exist parameter regions in which multiple attractors coexist. Typically, one of these attractors arises from periodically forced equilibrium, and therefore, is typically of small amplitude. On the other hand, the other attractors bifurcate from saddle node orbits, which tend to be of larger amplitude. Such bistable systems can have a simple manifold structure, but when considered in the presence of stochastic fluctuations, they may exhibit complex mixing between the bistable attractors, coupled with complicated looking transients between the basins.
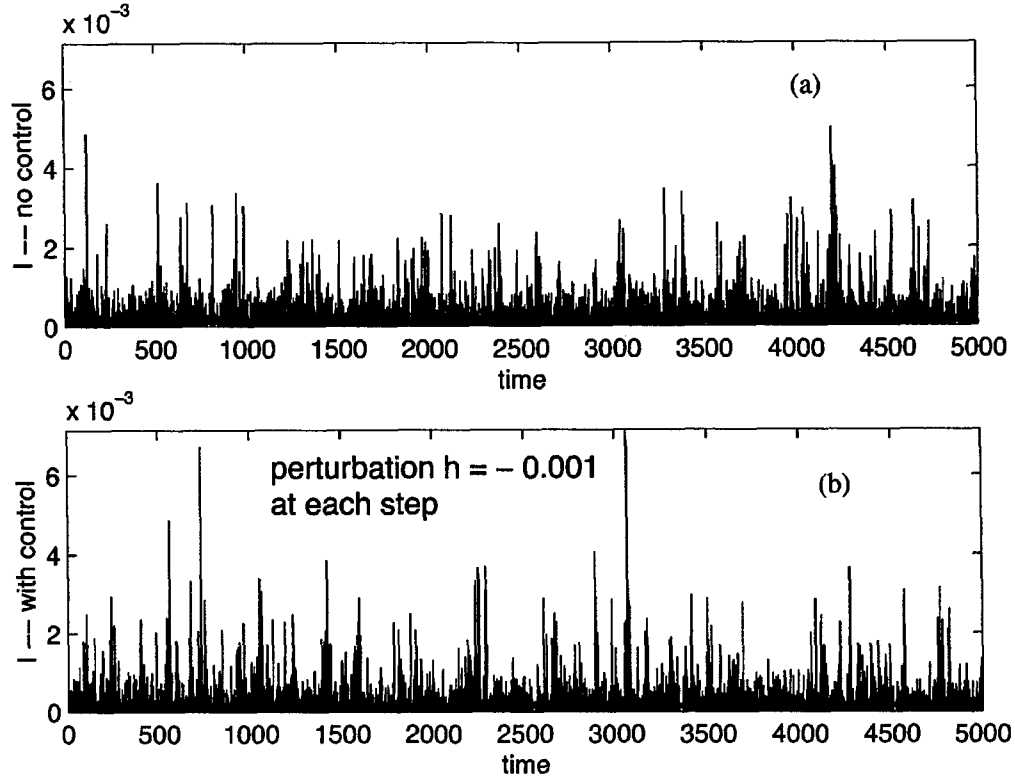
FIG. 3. (a) An uncontrolled time series of infective fraction as a function of time. (b) Constant vaccine control to reduce the rate of input of susceptibles.

By using the PDF flux, we are able to distinguish regions in the small amplitude basin that are quite sensitive to stochastic effects. We use this information in a control algorithm to prevent bursting dynamics (that is, to control stochastic chaos). It monitors this sensitive region and adjusts one physically relevant parameter to keep trajectories in the SA basin. This idea of monitoring a *loss region* has been used in other chaos control schemes that are deterministic (i.e., [28,29]). To our knowledge, we are not aware of any stochastic chaos control methods that account specifically for the emergent effects of stochastic perturbations.
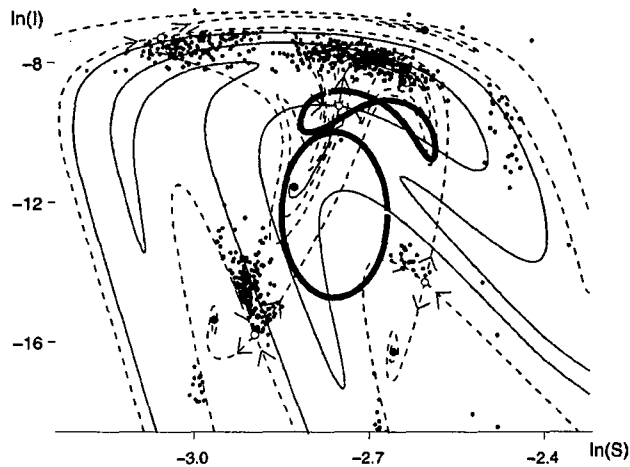

FIG. 4. Temporal average of those iterates leading to outbreaks in the next iterate using the same parameters as in Fig. 1. Notice the agreement with the spatial average in Fig. 3. The ellipse bounds the detection region. The figure eight curve is the image of the ellipse with controlled targeting.
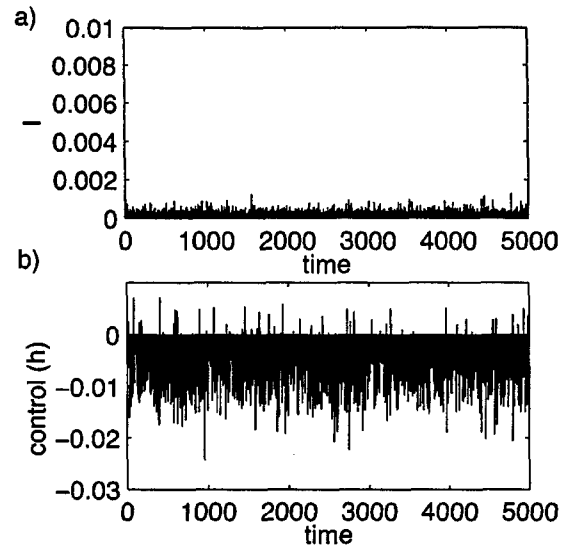

FIG. 5. Stochastic control to suppress large outbreaks in the MSI model. (a) Infectives with suppressed outbreaks due to control in the influx of infectives. (b) Perturbations h to the susceptible input rate μ in Eq. (4).
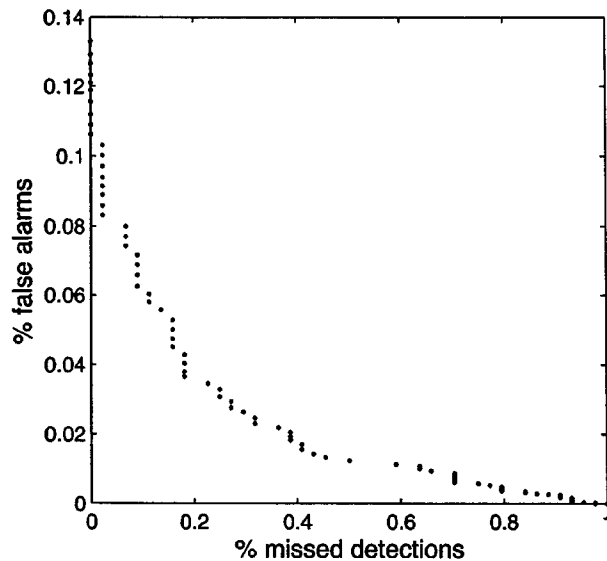
FIG. 6. A plot showing optimized predictability. Plotted are the false alarm rates versus missed detections.

One concern with a probabilistic detection scheme is that it is dependent on the choice of the monitoring region used for transition to an outbreak. Two issues with taking an actual time series and using the monitoring scheme above is that it may miss an outbreak that is there (missed detection), or it may predict an outbreak that does not occur. These statistics depend heavily on the size of the monitoring one uses. To see this in Fig. 6, we change the radius around of the center of the bull's eye and the radius around its preimage. Each dot plotted in Fig. 6 is for a different radius. The smallest radii are represented by the data points on the right. As we increase the radii, the data points move along the curve to the left. The false alarms are those outbreaks predicted by the bull's eye, but do not occur. The missed detection are the bursts that occur but are not predicted by the maximum flux hypothesis. It is the percentage not detected.

The choice we made for the detection region has solely been guided by time series observations and PDF flux predictions. It has not been optimized for the minimum number or size of perturbations. Because of the stochastic perturbations added to the system, the control measures will not "trail off" as in targeting unstable periodic orbits.

One very interesting aspect of the control perturbation is that the value of h is sometimes positive. This counterintuitive result may be explained since an increase in S is used to trigger an earlier, but smaller, outbreak. To understand this, we consider the MSI model, but transformed and scaled, so that the steady state equilibrium in the absence of forcing is now at the origin, and we examine the conservative system in the absence of damping as well [30],

$$x'(t) = -\nu y,$$
$$y'(t) = \nu x(1+y). \tag{11}$$

In Eq. (11), x is a scaled susceptible, y is a scaled infective, the equilibrium is at the origin, and the frequency ν is a function of the epidemiological parameters. Notice that since the population is assumed to be constant, inthe absence of any infectives [$y=-1$ in Eq. (11)], the fraction of susceptibles slowly increases. In addition, all oscillatory solutions must lie on level curves to the Lyapunov function: $V(x,y) = x^2 + 2y - 2 \ln(y+1)$.

Now suppose we have a small amount of infectives imposed by a strong level of vaccine. Then the infectives will stay small for a long period of time, until enough susceptibles grow to cause an outbreak of very large amplitudes by coming in contact with a few infectives [31]. That is, an outbreak will not occur unless the susceptibles reach a critical level in a long time scale while in the presence of a small fraction of infectives. To be specific, suppose $y=-1+c\epsilon$, where $c>0$ is constant. Then $y'=xc\epsilon$. If $x<0$, then the infectives decrease further, implying a much larger outbreak at a later time. Therefore, if one increases the infectives, the system fires sooner, with a smaller outbreak, since the infectives are pushed further away from the invariant line $y=-1$. When the control h is adjusted so that it is positive, the effect is to cause an increase in the rate of infectives, thus reducing the size of the outbreak.

Finally, although the vaccine control fluctuations do not decrease the mean incidence levels of infection, the control may be combined with tracking methods for epidemic control [26] to reduce the mean reproductive rate of infection below threshold to kill off the disease without causing unwanted outbreaks during vaccination.

ACKNOWLEDGMENTS

[1] Y. Moreno, R. Pastor-Satorras, and A. Vespignani, Eur. Phys. J. B **26**, 521 (2002).

[2] R. Pastor-Satorras and A. Vespignani, Phys. Rev. E **65**, 036104 (2002).

[3] R. M. Anderson and R. M. May, *Infectious Diseases of Humans—Dynamics and Control* (Oxford Science Publications, Oxford, 1991).

[4] B. M. Bolker and B. T. Grenfell, Proc. R. Soc. London, Ser. B **251**, 75 (1993).

[5] J. Patz, Proc. Natl. Acad. Sci. U.S.A. **99**, 12506 (2002).

[6] J. Patz, M. Hulme, C. Rosenzweig, T. Mitchell, R. Goldberg, A. Githeko, S. Lele, A. McMichael, and D. Le Sueur, Nature (London) **420**, 627 (2002).

[7] D. Rand and H. Wilson, Proc. R. Soc. London, Ser. B **246**, 179 (1991).

[8] L. Billings, E. Bollt, and I. Schwartz, Phys. Rev. Lett. **88**, 234101 (2002).

[9] D. Earn, P. Rohani, B. Bolker, and B. Grenfell, Science **287**,

67 (2000).

[10] E. H. Kaplan, D. L. Craft, and L. M. Wein, Proc. Natl. Acad. Sci. U.S.A. **99**, 10935 (2002).

[11] J. L. Aron, Theor Popul. Biol. **38**, 58 (1990).

[12] CDC, Morbidity and Mortality Weekly Report **38** (S-9), 7 (1989).

[13] V. N. Smelyanskiy and M. I. Dykman, Phys. Rev. E **55**, 2516 (1997).

[14] Z. Agur, L. Cojocaru, G. Mazor, R. Anderson, and Y. Danon, Proc. Natl. Acad. Sci. U.S.A. **90**, 11698 (1993).

[15] E. Bollt, L. Billings, and I. Schwartz, Physica D **173**, 153 (2002).

[16] I. Schwartz and H. Smith, J. Math. Biol. **18**, 233 (1983).

[17] L. Billings and I. Schwartz, J. Math. Biol. **44**, 31 (2002).

[18] A. L. Lloyd and R. M. May, J. Theor. Biol. **179**, 1 (1996).

[19] Z. Agur, Y. Danon, R. Anderson, L. Cojocaru, and R. May, Proc. R. Soc. London, Ser. B **252**, 81 (1993).

[20] I. Schwartz, J. Math. Biol. **21**, 347 (1985).

[21] The method may be applied continously by using compositions of the operator in Eq. (5). The results show no qualitative change from the discrete formulation Ref. [25].

[22] L. Arnold, *Random Dynamical Systems* (Springer-Verlag, New York, 1998).

[23] S. Wiggins, *Chaotic Transport in Dynamical Systems* (Springer-Verlag, New York, 1992).

[24] B. K. Kesdal and B. Oksendal, *Stochastic Differential Equations: An Introduction With Applications* (Springer-Verlag, New York, 2003).

[25] G. Froyland and K. Aihara, in Proceedings of the 1998 International Symposium on Nonlinear Theory and its Applications, Crans-Montana, Switzerland, 1998 (unpublished), Vol. 2, pp. 623–626.

[26] I. B. Schwartz and I. Triandaf, in *Predictability and Nonlinear Modeling in Natural Sciences and Economics*, edited by J. Grasman and G. vanStraten (Kluwer Academic, Dordrecht, The Netherlands, 1994), pp. 216–227.

[27] I. Schwartz, L. Billings, and E. Bollt (unpublished).

[28] W. Yang, M. Ding, A. J. Mandell, and E. Ott, Phys. Rev. E **51**, 102 (1995).

[29] I. B. Schwartz and I. Triandaf, Phys. Rev. Lett. **77**, 4740 (1996).

[30] L. Billings, E. Bollt, D. M. Morgan, and I. B. Schwartz, in *Fourth International Conference on Dynamical Systems and Differential Equations*, 2002, Special issue of Discrete Cont. Dyn. Syst. **9**, 123 (2003).

[31] It can be shown that if the infectives start as $y-1=O(\epsilon)$, and the susceptibles are small as well, then the peak size will be such that $y=O(\epsilon^{-1/2})$ [16].

Stochastic bifurcation in a driven laser system: Experiment and theory

Lora Billings
Department of Mathematical Sciences, Montclair State University, Montclair, New Jersey 07043, USA

Ira B. Schwartz and David S. Morgan
Naval Research Laboratory, Code 6792, Plasma Physics Division, Washington, D.C. 20375, USA

Erik M. Bollt
Department of Mathematics and Computer Science, and Department of Physics, Clarkson University, Potsdam, New York 13699, USA

Riccardo Meucci
Istituto Nazionale di Ottica Applicata, Largo E. Fermi 6, 50125 Firenze, Italy

Enrico Allaria
Department of Physics, University of Florence, Florence, Italy

We analyze the effects of stochastic perturbations in a physical example occurring as a higher-dimensional dynamical system. The physical model is that of a class-*B* laser, which is perturbed stochastically with finite noise. The effect of the noise perturbations on the dynamics is shown to change the qualitative nature of the dynamics experimentally from a stochastic periodic attractor to one of chaoslike behavior, or noise-induced chaos. To analyze the qualitative change, we apply the technique of the stochastic Frobenius-Perron operator [L. Billings *et al.*, Phys. Rev. Lett. **88**, 234101 (2002)] to a model of the experimental system. Our main result is the identification of a global mechanism to induce chaoslike behavior by adding stochastic perturbations in a realistic model system of an optics experiment. In quantifying the stochastic bifurcation, we have computed a transition matrix describing the probability of transport from one region of phase space to another, which approximates the stochastic Frobenius-Perron operator. This mechanism depends on both the standard deviation of the noise and the global topology of the system. Our result pinpoints regions of stochastic transport whereby topological deterministic dynamics subjected to sufficient noise results in noise-induced chaos in both theory and experiment.

I. INTRODUCTION

Noise-induced escape, which appears as a form of bifurcation in dynamical systems, is now documented in many areas of science and engineering [1]. It arises in stochastic processes, which we consider to be a composition of deterministic and time-dependent noisy systems. Detecting chaos in noisy systems is still an issue of debate. Efforts have been made to carry over operational definitions of deterministic chaos to stochastic systems, such as proving the existence of a positive Lyapunov exponent [2] and exploring the interaction of noise and a global bifurcation based on underlying unstable structures, such as a chaotic saddle [3]. Many of the underlying deterministic systems in these examples have parameter regimes in which multiple attractors give rise to noise-induced escape from one attractor to another. Such systems may be analyzed globally using the Hamiltonian theory of large fluctuations, or considering escape from attracting potential wells along most probable exit paths [4] using the theory of quasipotentials [5,6] or a variational formulation of optimal escape paths [7]. It is well known that noise can excite unstable chaotic structures while destroying regular periodic dynamics, but most studies consider noise-induced chaos occurring near a bifurcation, such as a saddle-node

point or a crisis of chaotic attractors that leave a chaotic saddle present.

In driven deterministic systems, the existence of chaotic invariant sets, such as chaotic saddles, can be proven by examining the topology of intersecting manifolds [8]. As an example, we cite the Melnikov method [9]. Although it has been extended to stochastic systems [10], it is limited in application since it is a bifurcation result that is perturbed from a global homoclinic or heteroclinic connection in a conservative system. Therefore, in many cases, one must rely on algorithmic methods for the numerical computation of unstable objects and their manifolds [11–13], with the hope that one may extract transverse intersections. We also note that in contrast to the hypothesis that noise-induced chaos is caused by a chaotic saddle excitation, a recent result shows that only partially formed manifold intersections (in which no chaotic saddle exists) may also be found to have a positive Lyapunov exponent [14].

In this paper, we compare a bifurcation observed in a nonequilibrium stochastic class-*B* laser experiment to a corresponding model of the system. We include experimental results, as well as the theoretical explanation of the observations. In particular, experiments support the claim that adding larger stochastic perturbations to the system results in qualitatively different dynamics. Using the model, we pro-
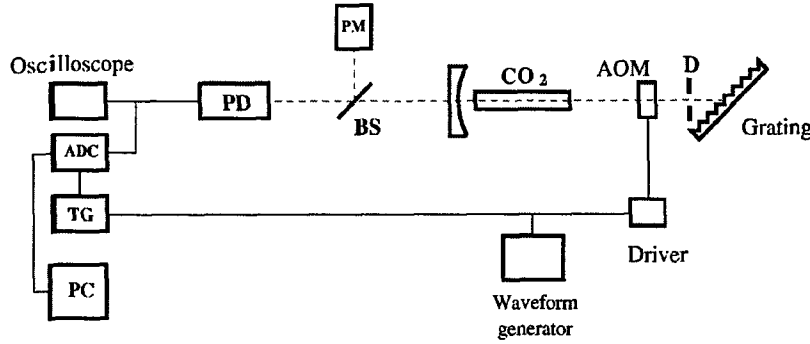
FIG. 1. Experimental apparatus used to perform our measurements. AOM, acousto-optic modulator; BS, beam splitter; PM, power meter; PD, photodetector; TG, trigger generator; ADC, analog-to-digital converter; and PC, personal computer.

vide evidence that this is an example of a bifurcation to noise-induced chaos by explicitly computing the probability transport due to noise. In this way, the interaction of noise and the underlying topology is identified in the emergent dynamics. We present analytic methods that specifically carry out the task of constructing the invariant density and transition probabilities in a rigorous manner to address the problem of this P-type stochastic bifurcation, as defined in [15]. Since it is a global approach, it is an alternative to using the Hamiltonian theory of large fluctuations, as described in [7,16] for autonomous systems, and in [17] for periodic systems. New tools were developed that are based on discrete approximations to the Frobenius-Perron operator with additive noise, defined as the stochastic Frobenius-Perron operator (SFPO) [18,19].

Using the SFPO, we identify the active regions of stochastic transport, or probability transitions, in the model. The advantage of this method is that we can find the probability density function (PDF) and maximal transport across boundaries in the absence of *a priori* knowledge of manifold structures and without time averaging. From the SFPO method, since one can directly compute the invariant density, spatially averaged Lyapunov spectra may be computed if the linear variation along an orbit is known. For stochastic systems that are sufficiently ergodic, spatial and temporal averages of the Lyapunov spectra are equal, and therefore, a positive Lyapunov exponent averaged spatially is a possible indicator of stochastic, or noise-induced, chaos [15].

To contrast our work from previous theories, we note that the bifurcation is far from parameters that would lead to a natural bifurcation to chaos, and large noise levels are included. Many studies in this field have relied on examining small noise limits, such as quasipotential theory [6] and optimal path theory [4], although this work has more recently been extended to the regime of finite noise intensity [20]. Underlying unstable fractal structures and noise-induced basin escape times have also been examined from quasipotential theory [6] for simple maps. The basin boundary in the system we study is a simple structure; i.e., it is nonfractal due to the lack of intersecting stable and unstable manifolds. In fact, only the forward crossings of a heteroclinic tangle could be identified, and no nonattracting chaotic sets are found to exist. The maximum Lyapunov exponent was calculated to increase smoothly through zero at the transition. Although both smooth and discontinuous onset are attributed to noise-induced chaos, the transition, which resembles a noise-induced attractor explosion described in [6], is not ob-

served. In fact, the transition is smooth statistically, evidenced by the smooth transition of a Lyapunov exponent through zero, which may be due to the noise-induced unstable dimension variability [21]. There is also a resemblance to noise-induced switching between multiple attractors as described in [3], but evidence provided by the probability density function supports the fact that trajectories spend as much time (if not more) near the partially formed heteroclinic tangle as the two periodic attractors. We also note that as previously reported in [6] and [3], both explosions and attractor switching are facilitated by fractal basin boundaries and nonattracting chaotic sets.

The layout of the paper is as follows. In Sec. II, we describe the experimental setup of a nonequilibrium stochastic class-B laser. We illustrate the effects of noise on the dynamics of the intensity and show how the structure of the attractor changes. In Sec. III, we briefly review the laser model of the experiment in a reduced form and show that it captures many of the features of the experiment. Section IV illustrates the effect of noise on the laser model and specifically shows how the maximal (or top) Lyapunov exponent depends smoothly on the standard deviation as it transitions from stochastic periodic behavior to stochastic chaos. The global structure of the underlying topology and transport results are presented in Sec. V, and the discussion is presented in Sec. VI.

II. AN ACOUSTICALLY OPTICAL MODULATED LASER EXPERIMENT WITH NOISE

To examine the effects of external noise in an experiment, we consider an acoustically optical modulated laser system. The experimental apparatus is shown in Fig. 1. It consists of a single-mode CO_2 laser with an intracavity acousto-optic modulator allowing modulation of the cavity losses. The optical cavity is 1.30 m long and the total transmission coefficient T is 0.10 for a single pass. The intensity decay rate $k(t)$ can be expressed as follows:

$$k(t) = k(1 + \alpha \sin^2\{B_0[1 + f(t)]\}), \qquad (1)$$

where $k = cT/L$, c is the speed of light in a vacuum, L is the cavity length, $\alpha = (1 - 2T)/2T$, B_0 is a bias, and $f(t)$ is the modulation signal,

$$f(t) = \beta \sin(2\pi\nu t) + \eta(t), \qquad (2)$$

with $\nu = 100$ kHz and the modulation amplitude β. The random variable η is considered to be normally distributed with
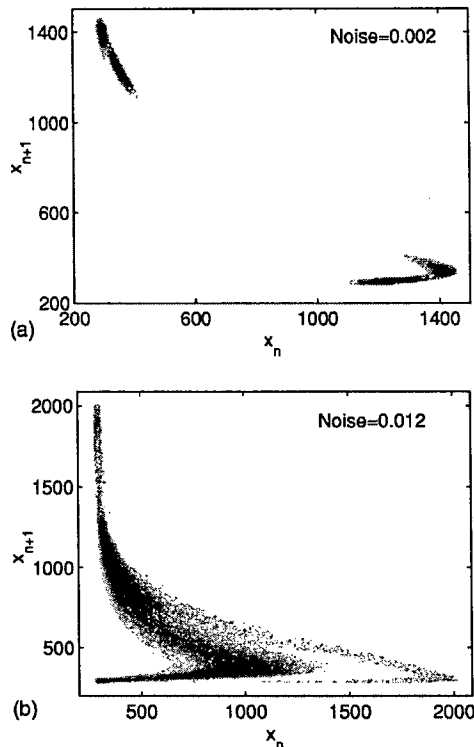
FIG. 2. Contour plots of the embedded intensity data (arbitrary units) under perturbations of η. Darker shades indicate regions visited with higher frequency. Small perturbations are used in the left graph, which result in a noisy periodic orbit. Larger perturbations are used in the right graph. Notice how the emergent dynamics are fundamentally different from the smaller case.

mean zero and standard deviation σ. The noisy signal $f(t)$ is provided by an arbitrary waveform generator (Tektronix Mod. AWG420), which generates both the sinusoidal signal and the random variable η using an independent internal Gaussian noise generator. Specifically, the noise is added periodically with the period of drive; i.e.,

$$\eta(t) = \eta_n \delta\left(t - \frac{n}{\nu}\right), \quad n = 1, 2, \ldots, \tag{3}$$

and δ is the Dirac delta function, and η_n is now a discrete random variable.

It is known that by increasing the amplitude modulation, the system undergoes a sequence of subharmonic bifurcations leading to chaos when $\eta = 0$ [22]. However, when noise is added to the system through the driver, the resulting dynamics is highly dependent on the noise amplitude. In Fig. 2, we see two examples of the output of the intensity plotted as a contour map of the embedded data for two values of the noise strength at the same value of the modulation amplitude $\beta = 0.360$. Note that darker shades indicate regions visited with higher frequency, and x_n is the local maximum of the measured intensity. The left panel shows the case where small noise results in a two-piece attractor. The deterministic attractor at this parameter value is periodic, located at the dark regions in the middle of the pieces. We describe this behavior as a noisy periodic attractor since its power spec-

trum is slightly broadened around the corresponding frequency. In the right panel, considerably more noise causes a qualitative change in the attractor. The periodic orbit is still located in the darkest regions of the graphs, but notice how there is significant sampling to other parts of the phase space not previously sampled at lower noise amplitudes. To understand the mechanism resulting in the stochastic bifurcation, we consider an accurate model of the experimental process.

III. AN AOM LASER MODEL

In [23], a multifrequency phase control on a two-level, two-dimensional CO_2 laser model produced both experimental and numerical evidence that it was able to preserve periodic behavior within a chaotic window as well as to reexcite chaotic behavior when it is destroyed by a crisis. In the model used, only intensity and population inversion were considered. To retain fidelity between theory and experiment, a more realistic four-level model of a CO_2 laser, which incorporated intensity, two resonant population levels, and two coupled rotational manifolds, was used in [24]. Analysis showed that an approximate reduction to three state variables could be made by examining differences in the resonant and rotational population levels while still retaining many of the global features of the bifurcations. Therefore, we begin our study of the scaled three-dimensional model in a stochastic version, where noise is added to the intensity equation. The variables have already been scaled to be dimensionless [24]. The driven three-dimensional system has the advantages that (i) it is higher dimensional than other models, and (ii) when sampled discretely at the drive frequency, its phase space can be visualized in three dimensions. The model equations are given by

$$y_1' = k_0(y_2 - 1 - \alpha \sin^2\{B[1 + f(t)]\}),$$

$$y_2' = -\gamma_1 y_2 - 2k_0 e^{y_1} y_2 + y_3 + P,$$

$$y_3' = -\gamma_2 y_3 + z y_2 + z P, \tag{4}$$

and

$$f(t) = A \sin(\omega t) + \eta(t), \tag{5}$$

where $\eta(t)$ is discretely modeled as in Eq. (3) with period $2\pi/\omega$, y_1 is the natural logarithm of the intensity, y_2 is the main population difference, and y_3 is the difference in rotational levels. The fixed parameters are $k_0 = 32.97$, $\alpha = 4$, $B = 0.21$, $\omega = 0.897\,597\,9$, $\gamma_1 = 10.0643$, $P = 0.082$, $\gamma_2 = 1.0643$, $z = 10$, and we vary A.

We now describe the topology of Eqs. (4) and (5) without stochastic perturbations, i.e., $\eta(t) \equiv 0$. As shown in the bifurcation diagram in Fig. 3, periodic orbits are represented as a function of A. As A is increased, a period-one attractor proceeds through a period-doubling bifurcation. Several saddle-node bifurcations for varying periodic orbits also occur, which will play a role when noise is turned on. We show the first saddle node, which is of period three in the figure. Therefore at $A = 0.214$, there exists an interval of bistability I_A, formed by period-four and period-three attractors. Asso-
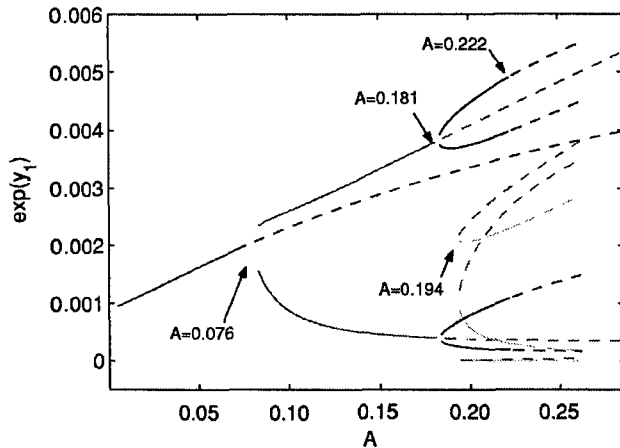
FIG. 3. (Color online) The bifurcation diagram for the laser model as a function of the forcing amplitude. Plotted are branches of both stable and unstable periodic orbits. The y axis is scaled intensity. The parameters are given in the text.

ciated with the period-four attractor is an unstable period-two saddle orbit (which is a flip saddle) and an unstable period-one flip saddle orbit from the period-doubling bifurcation. The period-three attractor has an associated unstable period-three regular saddle orbit arising from a saddle-node bifurcation. We hypothesize that the multi-instability in this system when $A \in I_A$ has the topological structure needed to induce chaoslike behavior with additive stochastic perturbations. Since the bifurcation diagram contains only stability and amplitude information, we explore the phase space through numerical simulation. (Rigorous analysis of the onset of the saddle-node bifurcation, which leads to bistable regions, is similar to that done in [25] and will be presented elsewhere.)

IV. STOCHASTIC DYNAMIC SIMULATIONS

In keeping with the experimental setup, we model the stochastic system as a discrete dynamical system. Since the experimental system was forced periodically with discrete noise using Eq. (3), we can add the perturbations at the same period as that of the drive given by Eq. (5). Consider the periodic sampling as discrete time events of a deterministic system. We add the perturbations to initial conditions, similar to adding noise to a discrete map. In general, we consider stochastically perturbing a function F with additive noise: $F: \mathbb{R}^3 \to \mathbb{R}^3$, $x \mapsto F(x) + \eta$, where η is an identically independently distributed random variable with normal distribution and mean $=0$ applied once each iteration. Since we are most interested in the situation where small noise amplitude can have major global consequences, we focus on the case where the random part η is assumed to be independent of state x and relatively small, so that the deterministic part F has primary influence. We add the perturbation to each component independently and set the standard deviation $\Sigma = \text{diag}(\sigma_1, \sigma_2, \sigma_3)$ as a parameter. This standard deviation is relative to the normalized scaling of the *almost*-compact space we consider. That is, each σ_n is scaled as if the phase

space is a unit box in three dimensions. With no noise, the only observable behavior is asymptotically periodic trajectories converging to the period-three or period-four orbits. By adding noise with increasing standard deviation, a random trajectory changes from a noisy periodic orbit to chaoslike deterministic behavior, visiting the two periodic orbit basins.

We remark that although in the original unscaled model, noise is added multiplicatively, it is approximately equivalent to adding noise additively in the scaled model from Eq. (4). This is due to the fact that the intensity of the original model is represented by the logarithm of the intensity in Eq. (4) [26]. The noise source appears as a term of the form $\sin^2\{B[1 + A \sin(\omega t) + \eta(t)]\}$. Taking a Taylor series expansion with respect to η yields a noise term on the order of η, which is independent of the state variables. Since the model is based on the natural logarithm of the intensity, a good approximation to the noise source is that the intensity equation has an additive noise term.

In quantifying underlying complex determinism in stochastic systems, it is inherently difficult to draw a clear line to distinguish between complex oscillations due to significant contributions from deterministic parts influenced by noise and a large noise amplitude effect wherein complex oscillations are primarily due to random Brownian diffusion. One necessary, but not sufficient, condition for the existence of chaos is the calculation of positive Lyapunov exponents. Lyapunov exponents measure the average rate of separation of neighboring initial points. Because we are adding perturbations to this system discretely, we can find a finite-time numerical approximation for the Lyapunov exponents of the map using the linear variational equations of the original system on the Poincaré section. A positive Lyapunov exponent can identify chaotic behavior, but diffusion can yield a positive Lyapunov exponent as well [27]. Since chaos is also associated with the underlying topology of the manifolds of the dynamical system, we examine the unstable structures in the deterministic model and observe how they interact with the stochastic source terms. Specifically, we would like to identify the structures in the original phase space that noise can excite. For example, if noise causes a trajectory to visit a chaotic saddle, then there should be locally unstable contributions to the Lyapunov spectrum. If enough of the unstable contributions are sampled, then the topology underlying the chaotic saddle will be reflected in an increasing maximum exponent.

In modeling the experiment, we consider additive stochastic perturbations to the first component, setting $\sigma_2 = \sigma_3 = 0$. The phase space projection of the attractor changes qualitatively as a function of the standard deviation, as we saw earlier. However, in Fig. 4, we show how the experiment and model both appear to change smoothly as the standard deviation increased. This is reflected in the time-averaged Lyapunov exponent computations. That is, as we increase σ_1 away from zero, the Lyapunov exponent increases and has a smooth transition from negative to positive values, as shown in Fig. 5. The crossing is near $\sigma_1 = 0.064$. As an example, we graph two trajectories to show the emergent dynamics in the three-dimensional phase space in Fig. 6. Setting $\sigma_1 = 0.04$, the largest Lyapunov exponent is negative, predicting noisy periodic behavior, as seen near the period-four orbit. Setting
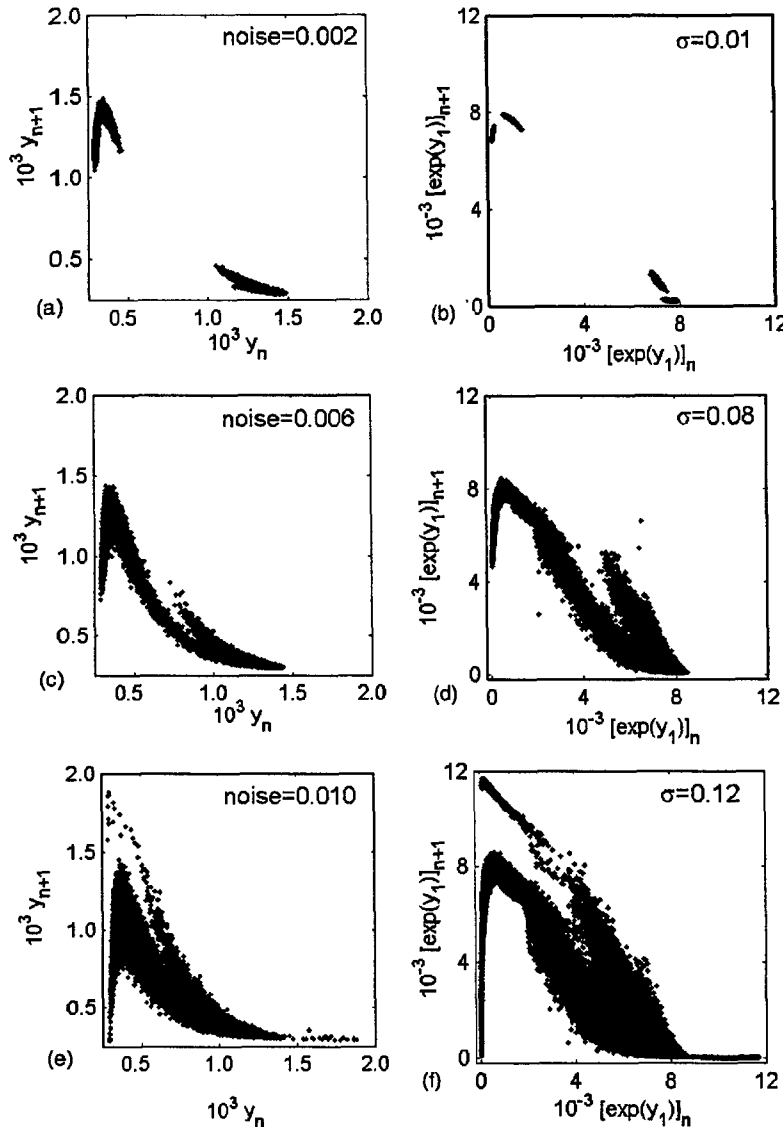
FIG. 4. The left graphs show intensity data (arbitrary units) for increasing perturbations of η. The right graphs show similar results for the model given by Eq. (4). Plotted are successive local maxima of the intensity values. Notice that in both cases, the attractors go from a stochastically perturbed period-four cycle, through a basin hopping attractor, and then to bursting among several basins of attraction from the deterministic case.

$\sigma_1 = 0.16$, the largest Lyapunov exponent is positive, predicting chaoslike behavior.

More detail about the dynamics can be obtained by calculating the bursting statistics as a function of the standard deviation of the noise. We approximate the burst rate by
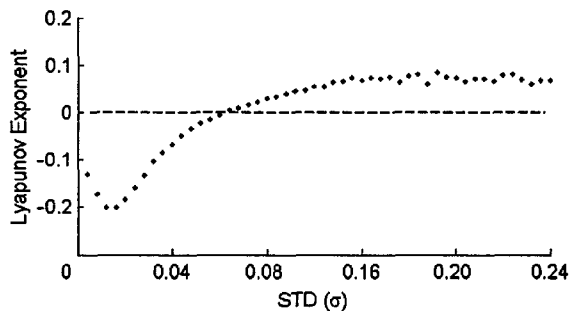

FIG. 5. The largest Lyapunov exponent as a function of the standard deviation of the noise. The transition from negative to positive values is smooth, as predicted in [21].

setting a threshold for e^{y_1} at 0.009. This value was determined by monitoring a trajectory with no noise. For each standard deviation value, we count the number of points in a random trajectory above the threshold and divide by the total number of points. See Fig. 7 for the results using trajectories 700 000 points long. Notice how bursting occurs for $\sigma > 0.12$. This value is different from the bifurcation value predicted by the Lyapunov exponent. Therefore, we will investigate the stochastic dynamical system as the noise parameter σ is varied.

Experimentally, we observe and show in Fig. 6 the changes that occur as σ varies. There exists a two-piece noisy period-four attractor for $\sigma < 0.064$. Then, the two pieces join into one attractor for $0.064 < \sigma < 0.12$, which is reflected by a positive Lyapunov exponent. Then, the trajectories start to burst and visit the period three. This statistic is not noticeable until $\sigma = 0.12$. The amount of bursting is reflected in the burst rate. For $0.064 < \sigma < 0.12$, the noise provides the transport for the trajectories to visit the stable period-four orbit, the unstable period-two orbit, and the unstable period-one orbit. But for $\sigma > 0.12$, the trajectory visits
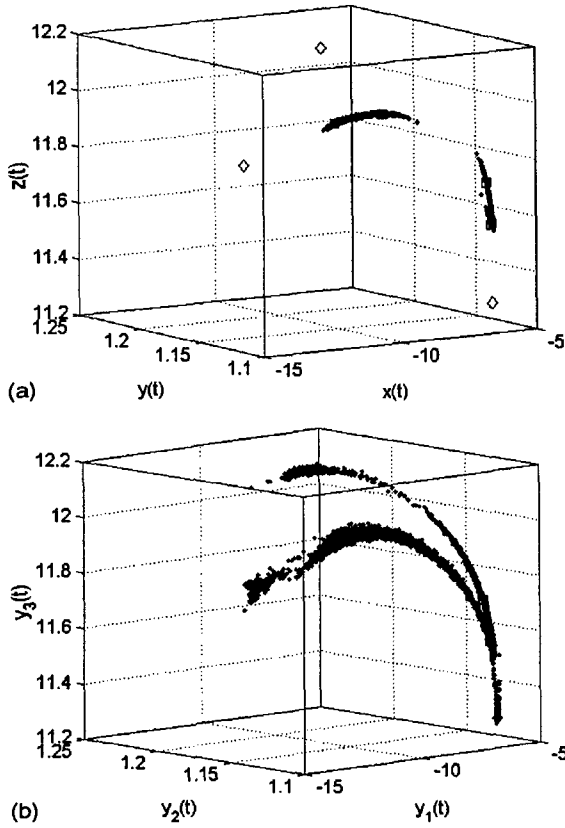
FIG. 6. The left graph shows noisy periodic behavior generated by the system when the standard deviation of the noise is σ_1 =0.04. This is the behavior predicted by a negative Lyapunov exponent. The right graph shows chaoslike behavior generated by the system when σ_1=0.16. This is the behavior predicted by a positive Lyapunov exponent in Fig. 5.

both the period-three and period-four attractors, and the manifolds in between them. See the right graph in Fig. 6 as an example. We will now explore these dynamical changes by a transfer operator-based analysis, and we will compare the results to the topology of the stable and unstable manifolds of the corresponding deterministic system and interpret the influence of the added noise.
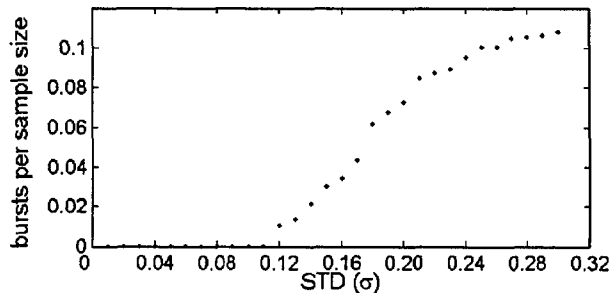

FIG. 7. The burst rate as a function of the standard deviation of the noise. Notice that the bursting increases from zero near σ =0.12.

V. PHASE-SPACE ANALYSIS OF STOCHASTIC DYNAMICS

Understanding the interaction between noise and the deterministic topology requires that we examine the structure of the stable and unstable manifolds of the relevant saddles in the prechaotic regime. Locating stable and unstable manifolds can be done in several ways [11,12]. We use the box algorithm from [13] and describe it here briefly. By picking a box containing the unstable saddle with part of its stable and unstable manifolds, we can determine initial conditions that will generate trajectories remaining in the box for a large number of iterations. We then eliminate any points converging to an attractor. The initial conditions remaining in the punctured box approximate the union of the stable manifolds, while the last point of the trajectory that remains in the box approximates the unstable manifolds. This algorithm was used to generate the stable and unstable manifolds in Fig. 8.

As shown in Fig. 8, the two-dimensional stable manifolds of the period-three saddle orbit form the basin boundary between the period-three basin and period-four basin. The one-dimensional unstable manifolds approach the period-four orbit, intersecting the two-dimensional stable manifolds of the period-two and period-one saddles. This forms a forward connection of a heteroclinic tangle in R^3. There are no reverse connections or intersections of the stable manifolds of the period-three saddle orbit, which would be necessary for fully developed chaos.

By adding stochastic perturbations with a large enough standard deviation, random trajectories frequently escape their asymptotic limit toward one of the attracting periodic orbits and visit the other. In contrast to basin hopping, the trajectories spend a significant amount of time in between the two attractors, near the forward connections of the heteroclinic tangle. Essentially, short visits to the other basin act like a reverse connection, completing the tangle and enabling chaoslike behavior. Therefore, the trajectory follows the chaoslike dynamics in the time spent in between the two attractors. As the standard deviation of the noise is increased, this reverse jump occurs more frequently and more time is spent in between the attractors. These events can be identified by bursting, and the chaoticlike behavior is captured by both the Lyapunov exponent and burst-rate statistics.

What we wish to identify here is where the noise facilitates the reverse jump in phase space and provide evidence that the phenomenon is similar to a heteroclinic tangle. We begin by analyzing the time-series data. In Fig. 8, the point before the trajectory switches basins (defined in the noise-free case) is recorded. It is clear that the jumps occur frequently in three regions near the unstable period-three saddles. To quantify these regions, we calculate the Galerkin transport matrix.

The Galerkin transport matrix can be used as a tool to identify transport between the original basins as a function of the standard deviation of the noise added to the system [18]. Let $\nu(x)$ be the distribution of the random variable η,

$$\nu(x) = e^{-(x^T\Sigma^{-1}x)/2}/\sqrt{(2\pi)^3 \det(\Sigma)}. \qquad (6)$$

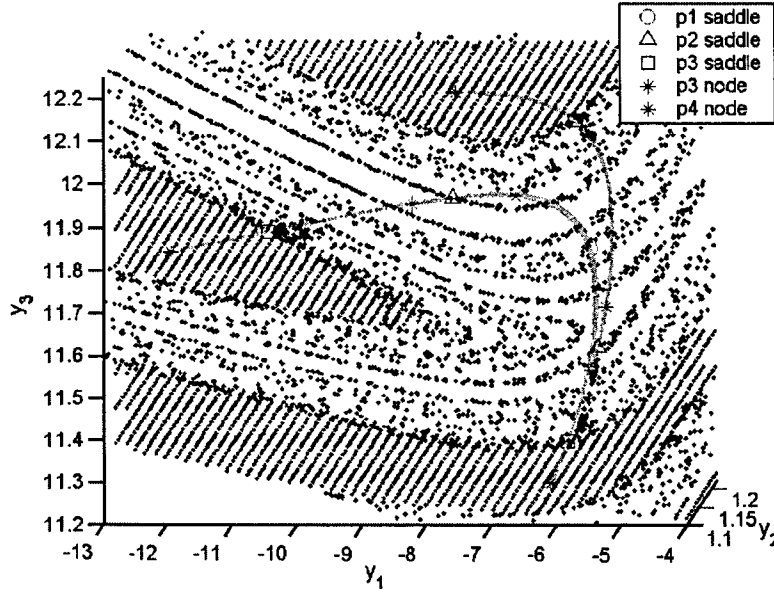As a spatial approximation, we use the SFPO in the form

FIG. 8. (Color online) The period-three basin is denoted by stripes and the rest of the space is the period-four basin. The union of the stable manifolds in the phase space is approximated by small dots in the period-four basin. This includes the stable manifolds for the period-one and period-two orbits. The union of the unstable manifolds is the solid curve with the period-three stars at the ends. The boundary between the period-three and period-four basins is formed by the stable manifold of the period-three saddle (squares). Notice how the unstable manifolds of the period-three saddle intersect the stable manifolds inside the period-four basin, forming the forward connections of the heteroclinic tangle. Superimposed is the time-series approximation of the flux from the period-four to the period-three basin in large dots.

$$P_{F_\nu}[\rho(\mathbf{x})] = \int_{\mathbb{R}^3} K(\mathbf{x},\mathbf{y})\rho(\mathbf{y})d\mathbf{y}, \qquad (7)$$

where the stochastic kernel describing the PDF of the noise perturbation is $K(\mathbf{x},\mathbf{y})=\nu(\mathbf{x}-F(\mathbf{y}))$. Assuming a nonzero external noise is added in each component, Eq. (7) becomes

$$P_{F_\sigma}[\rho(\mathbf{x})] = \frac{1}{\sqrt{(2\pi)^3\det(\Sigma)}}\int_{\mathbb{R}^3} e^{-(\mathbf{x}-\mathbf{y})^T\Sigma^{-1}(\mathbf{x}-\mathbf{y})/2}\rho(\mathbf{y})d\mathbf{y}. \qquad (8)$$

Note that although it is possible to let any of the standard deviations tend to zero in the SFPO where the kernel limits to a delta function, it is more realistic to approximate the zeros by very small values. This is due to the fact that the experiment is always perturbed by small noise. Since we require a finite dimension for computation, we cover the phase space with N disjoint boxes B_i and choose a set of basis functions to be the family of characteristic functions

$$\phi_i(x) = \begin{cases} 1 & \text{if } x \in B_i \\ 0 & \text{if } x \notin B_i. \end{cases} \qquad (9)$$

In principle, any set of basis functions of L^2 can be used, but we use characteristic functions to help us locate spatial transport, as was motivated historically by Ulam's method. The approximation of the Frobenius-Perron operator projects to a $N\times N$ matrix, called the Galerkin transport matrix (GTM),

$$A_{i,j} = (P_{F_\sigma}[\phi_i],\phi_j) = \int_{\mathbb{R}^3} P_{F_\sigma}[\phi_i(\mathbf{x})]\phi_j(\mathbf{x})d\mathbf{x}, \quad 1 \le i,j \le N. \qquad (10)$$

The GTM describes the mass flow from one box to another over one iteration. That is, the entry for $A_{i,j}$ approximates the percentage of box i that iterates to box j under the stochastic map. Then partition the boxes according to their basin and reorder the GTM by similarity transformations to reflect that

partition. In theory, the case with no noise will result in a block-diagonal matrix, reflecting dynamics in the disjoint basins. Under stochastic perturbations, the GTM approximates three things: (i) the off-diagonal blocks indicate where the transport between basins occurs—this is the mass flux (or simply flux), (ii) the dominant eigenvector having eigenvalue unity approximates the PDF, and (iii) by weighting the mass flux by the PDF, we pinpoint regions in phase space that have the greatest probability of leakage into another basin—this is the area flux. See [19,18] for details.

We show the GTM approximation of the PDF in Fig. 9. Since the noise distribution is assumed to be normal, it is expected that the PDF has nonzero entries everywhere in phase space. However, many of these values are sufficiently small so that when added to unity, they make zero contribution due to the fact they are below machine error. Therefore,
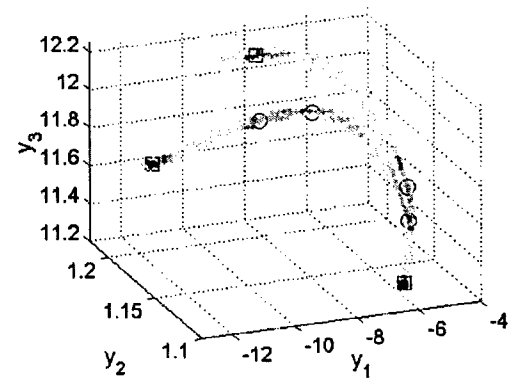

FIG. 9. An approximation by the GTM of the PDF when σ_1 =0.16. The squares represent the stable period-four orbit. The circles represent the stable period-three orbit. The darker shades indicate regions with the highest probability. Notice that they occur near the stable periodic orbits, but there is structure connecting these regions called the stochastic chaotic saddle. As σ increases, orbits spend more time on the chaotic saddle, indicating the increased frequency of bursting dynamics.
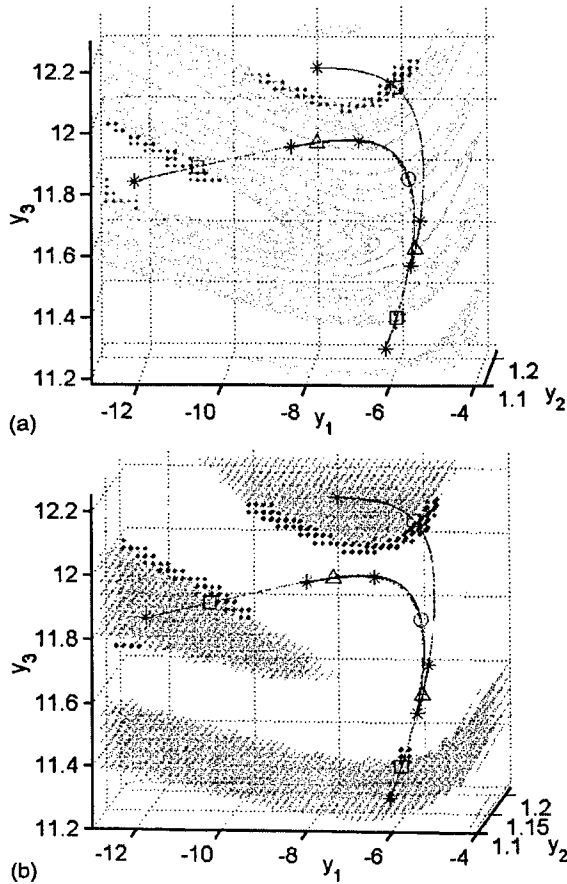
(a)

(b)

FIG. 10. (Color online) Approximation of the transport from the GTM when $\sigma_1 = 0.16$. (a) shows regions of most active transport from the period-three to the period-four basin in large dots. (b) shows regions of most active transport from the period-four to the period-three basin. Notice that these regions occur near the period-three saddle orbit represented by the squares. In (a), the union the stable manifolds is displayed in layered sheets and unstable manifolds form the one-dimensional curve with the period-three points (stars) at the ends. They are approximated by the box algorithm from [13]. The stable manifolds of the period-three saddle form the basin boundary between the two basins. In (b), the basin of the period-three orbit is represented by the small dots. Also shown in both (a) and (b) are the stable period-four orbit (stars), the unstable period-two orbit (triangles), and the unstable period-one (circle).

we choose a numerical threshold of machine precision as a lower bound and replace all smaller values to zero in the PDF. Notice that as we add stochastic perturbations to the system, the most frequently visited regions lie near the unstable manifolds of the period-two and period-one saddle orbits from the noiseless case.

We observe that as the standard deviation is increased, the PDF spreads and crosses into the period-three basin, and through the stable manifold of the period-three saddle. This is evidence that there is the topology for a trajectory to emulate chaoslike behavior. We now will verify the fact that the trajectory actually uses these regions for transport. This is supported by the area flux, which is shown in Fig. 10. The
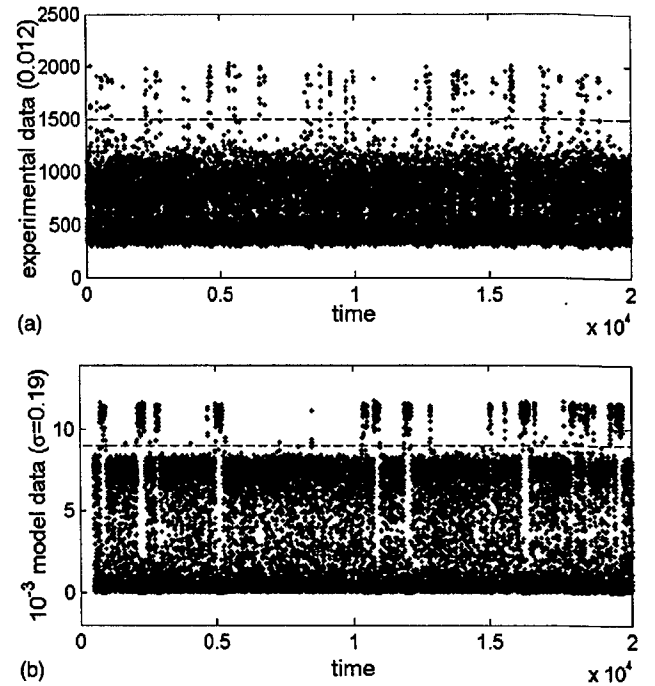

FIG. 11. Bursting time series from the experiment (a) and model (b). The dashed line indicates the threshold used to determine a burst.

regions where the trajectory is most likely to switch basins are found by multiplying the mass flux by the associated PDF value for that region of phase space. Notice the agreement between the transport region predicted by the time series in Fig. 8 and the area flux from the period-four to the period-three basin.

VI. DISCUSSION

Dynamics with noise is always present in experiments at least at some level. In many cases, noise is sufficiently small so that its role is ignorable with respect to the underlying determinism. However, even relatively low-amplitude noise may play a significant role in which the dynamics takes on a qualitative change that is different from the deterministic structure. In the physical example presented here, we have examined an experiment where noise has been injected into a modulated laser. The amplitude of the noise was adjusted, and the laser was seen to go from stochastically perturbed periodic behavior to one of stochastic-induced chaoslike dynamics. Because discrete control of the random noise amplitude could be achieved, the system was therefore analyzable by a discrete-map approach, thereby revealing explicitly the interaction of noise and the underlying deterministic topology.

In conjunction with the laser experiment, we have examined a quantitative model with additive noise in the intensity. Both exhibit similar bursting behavior, as shown in the time series data in Fig. 11. Although the topology of the experimental dynamics is difficult to ascertain, the quantitative nature of the model does allow an in-depth view of the under-
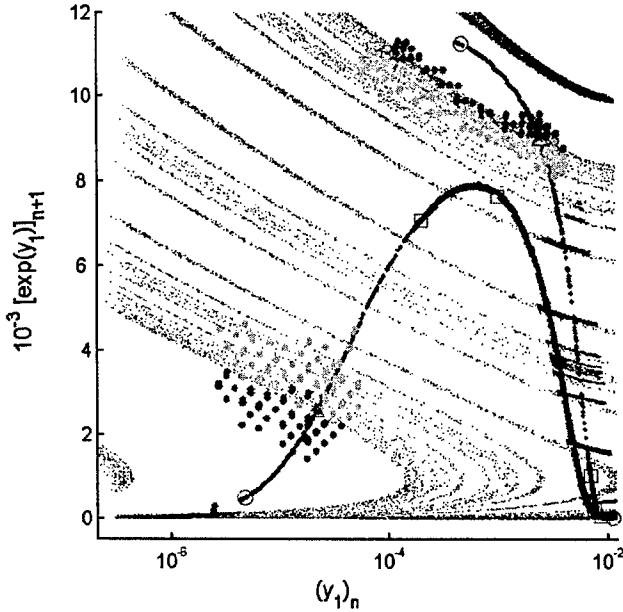
FIG. 12. (Color online) The return map of the fixed points corresponding to the periodic orbits and their projected manifolds. (The x axis has been plotted logarithmically to show more detail.) The unstable manifolds form the dark solid curve in the middle, while the stable manifolds are approximated by smaller points. In addition, the projected regions of transport are overlaid in large dots. Notice that the transport between the two basins predicted by the GTM in Sec. V lies close to the period-three saddles (triangles) on the stable manifold. The other periodic orbits are labeled as follows: period two, stars; period four, squares; period one, large dot; period-three node, circles; period-three saddle, triangle. The value of the standard deviation used was $\sigma_1 = 0.04$.

lying topology and its relation to noise. In the absence of noise, the topology of the system was determined, and the structure of the stable and unstable manifolds was computed in a prechaotic regime. When noise is added, the structure of the topology interacts with the stochastic fluctuations in such a way to induce chaoslike behavior, which is the emergent structure observed in both theory and experiment as shown in Fig. 4. The stochastic dynamics is the union of local stochastic dynamics within each basin and the dynamics near a partially formed chaotic saddle. For sufficiently large noise amplitudes, local instability near the manifold structure contributes to the time- and space-averaged linear variation so that the Lyapunov exponent becomes positive, which we take as criteria for stochastic bifurcation as defined in [15], and exemplified in [2].

In tying together the dynamics from the model and experiment, we can project the phase portrait of the transport and manifold structure to a lower dimensional return map, as we did in Sec. IV. In Fig. 12, we have depicted the fixed points that correspond to the unstable periodic orbits and their manifolds. Notice that because we used the box algorithm of [13], the manifolds are not grown from a saddle, but reflect the union of all such manifolds in the region we considered. The stable manifold (in black) corresponds to the basin boundary in the original phase space separating the bistable attractors in the deterministic case. In the projection

in Fig. 12, we can see where the maximum probability of transport from one basin to another occurs. Notice that much of it takes place near the basin boundary saddle points. That is, the period-three saddle stable manifold, which forms the basin boundary, intersects the regions of maximal probability transport. The stochastic dynamics fluctuates until it comes near the basin boundary, at which point it is attracted to the saddle point. Noise then takes on a dominant role, where the intensity is either pushed across the basin boundary, or remains in the same basin. The unstable manifold then dominates the noise, by pushing the dynamics further into the respective basin.

Our model of the class-B laser includes more physics in the problem, which in turn, leads to a more interesting class of dynamical behavior. Most laser models consist of just two population levels, describing the change in the population inversion and intensity. The advantage of such a model is that it may be studied in the plane, having one-dimensional stable and unstable manifolds. The resulting stochastic analysis could be compared directly to manifolds that were built from curve-following methods in the plane. In contrast, the model considered here is based on a four-level model, which agrees quantitatively with the experiment over a large range of values. The model requires two main levels and two rotational levels, resulting in a five-dimensional system of differential equations. Approximating the relaxation rates of the vibrational states by their average allows one to reduce the model to the current three-dimensional driven case [24]. The main difference here is that the stable manifolds are no longer one-dimensional. (The unstable manifolds are one-dimensional, however.) Here, two-dimensional stable manifolds are pierced by one-dimensional unstable manifolds. Therefore, regions of transient behavior may wander over a greater region of phase space in both the deterministic and stochastic models, offering a richer set of dynamical behavior than the two-level laser model.

One of the main conclusions of the current stochastic analysis is that maximal transport from one basin to another may not occur near the basin boundary saddles. Similar examples based on asymptotic properties of problems of escape where the phenomenon of saddle avoidance occurs can be found in [28,29]. We note that the methods used here not only agree with the previous local theories, but is an alternative to describe the global structure of the transport as well [18].

In general, computing stable and unstable manifolds is a difficult task, compounded here by the fact that the manifolds are of different dimensions. The technique used in this paper cannot grow the manifolds from a given saddle. Therefore, the global analysis of the four-level laser system lacks some of the precision of the two-level system. On the other hand, the SFPO tool does not require the manifold constructions a priori. Rather, the transport requires a partition of the basins of attraction in the zero noise case. When noise is added, the phase space is reconstructed in terms of transport across the referenced basin boundaries, and thus must contain components of the basin manifolds, regardless of their dimension.

In terms of model development, much work on noise had been done on maps in the plane, or two-dimensional flows.

In this paper, we have presented a stochastic experiment as well as a quantitative model that simulates the stochastic dynamics. The model is itself a reduction of a previously more complicated model [24], but nonetheless, captures the relevant features of the stochastic dynamics. In particular, it captures the interaction of the stochastic dynamics with the underlying topology of the model. This quantifies the smooth change of regular stochastic behavior to a bursting type of behavior between basins, which appears to be chaoslike in

that there exists a smooth transition from negative to positive Lyapunov exponents.

[1] N. G. van Kampen, *Stochastic Processes in Physics and Chemistry*, Lecture Notes in Mathematics Vol. 888 (North-Holland, Amsterdam, 1981).

[2] N. S. Namachchivaya and N. Ramakrishnan, J. Sound Vib. **262**, 613 (2003).

[3] S. Kraut, U. Feudel, and C. Grebogi, Phys. Rev. E **59**, 5253 (1999).

[4] M. Freidlin and A. Wentzel, *Random Perturbations in Dynamical Systems* (Springer-Verlag, Berlin, 1984).

[5] R. Graham and T. Tel, Phys. Rev. Lett. **52**, 9 (1984).

[6] A. Hamm, T. Tél, and R. Graham, Phys. Lett. A **185**, 313 (1994).

[7] R. S. Maier and D. L. Stein, Phys. Rev. E **48**, 931 (1993).

[8] J. Guckenheimer and P. Holmes, *Nonlinear Oscillations, Dynamical Systems, and Bifurcations of Vector Fields* (Springer-Verlag, New York, 1983).

[9] S. Wiggins, *Chaotic Transport in Dynamical Systems* (Springer-Verlag, New York, 1992).

[10] M. Frey and E. Simiu, Physica D **63**, 321 (1993).

[11] B. Krauskopf and K. Green, J. Comput. Phys. **186**, 230 (2003).

[12] B. Krauskopf and H. Osinga, Chaos **9**, 768 (1999).

[13] I. Triandaf, E. M. Bollt, and I. B. Schwartz, Phys. Rev. E **67**, 037201 (2003).

[14] L. Billings and I. B. Schwartz, J. Math. Biol. **44**, 31 (2002).

[15] L. Arnold, *Random Dynamical Systems* (Springer-Verlag, New York, 1998).

[16] M. I. Dykman, P. V. E. McClintock, V. N. Smelyanski, N. D.

Stein, and N. G. Stocks, Phys. Rev. Lett. **68**, 2718 (1992).

[17] J. Lehmann, P. Reimann, and P. Hanggi, Phys. Rev. Lett. **84**, 1639 (2000).

[18] L. Billings, E. M. Bollt, and I. B. Schwartz, Phys. Rev. Lett. **88**, 234101 (2002).

[19] E. M. Bollt, L. Billings, and I. B. Schwartz, Physica D **173**, 153 (2002).

[20] A. Bandrivskyy, S. Beri, and D. G. Luchinsky, Phys. Lett. A **314**, 386 (2003).

[21] Y. C. Lai, Z. Liu, L. Billings, and I. B. Schwartz, Phys. Rev. E **67**, 026210 (2003).

[22] F. T. Arecchi, R. Meucci, G. Puccioni, and J. Tredicce, Phys. Rev. Lett. **49**, 1217 (1982).

[23] I. B. Schwartz, I. Triandaf, R. Meucci, and T. W. Carr, Phys. Rev. E **66**, 026213 (2002).

[24] R. Meucci, D. Cinotti, E. Allaria, L. Billings, I. Triandaf, D. Morgan, and I. B. Schwartz, Physica D **189**, 70 (2004).

[25] T. W. Carr, L. Billings, I. B. Schwartz, and I. Triandaf, Physica D **147**, 59 (2000).

[26] For $y_1 = \ln x_1$, the original model defines $x_1' = k_0(y_2 - 1 - \alpha \sin^2\{B[1+f(t)]\})x_1$, where the noise is multiplicative. The change of variables results in $y_1' = k_0(y_2 - 1 - \alpha \sin^2\{B[1 + f(t)]\})$, as described in the scaled model in Eq. (4).

[27] J. B. Gao, C. C. Chen, S. K. Hwang, and J. M. Liu, Int. J. Mod. Phys. B **13**, 3283 (1999).

[28] Z. Schuss and A. Spivak, Chem. Phys. **235**, 227 (1998).

[29] D. G. Luchinsky, R. S. Maier, R. Mannella, P. V. E. McClintock, and D. L. Stein, Phys. Rev. Lett. **82**, 1806 (1999).